Aircraft Engineering and Aerospace Technology, Available online 11 July 2024
DOI:10.1108/AEAT-03-2023-0070

Installed nacelle aerodynamics at cruise and windmilling conditions

Francisco Sánchez-Moreno[1], David G. MacManus[1], Fernando Tejero[1], Josep Hueso-Rebassa[1] and Christopher Sheaf[2]

[1]*Centre of Propulsion and Thermal Power Engineering, School of Aerospace, Transport and Manufacturing, Cranfield University, Bedford, United Kingdom, MK43 0AL*

[2]*Rolls-Royce plc., P.O. box 31, Derby, United Kingdom, DE24 8BJ*

Abstract

Purpose – The decrease in specific thrust achieved by Ultra-High Bypass Ratio (UHBPR) aero-engines allows for a reduction in specific fuel consumption. However, the typical associated larger fan size might increase the nacelle drag, weight and the detrimental interference effects with the airframe. Consequently, the benefits from the new UHBPR aero-engine cycle may be eroded. This research evaluates the potential improvement in the aerodynamic performance of compact nacelles for installed aero-engine configuration.

Design/methodology/approach – Drooped and scarfed non-axisymmetric compact and conventional nacelle designs were down selected from a multi-point CFD-based optimization. These were computationally assessed at a set of installation positions on a contemporary wide-body, twin-engine transonic aircraft. Both cruise and off-design conditions were evaluated. A thrust and drag accounting method was applied to evaluate different aircraft, powerplant and nacelle performance metrics.

Findings – The aircraft with the compact nacelle configuration installed at a typical installation position provided a reduction in aircraft cruise fuel consumption of 0.44% relative to the conventional architecture. However, at the same installation position, the compact design exhibits a large flow separation at windmilling conditions that is translated into an overall aircraft drag penalty of approximately 5.6% of the standard cruise net thrust. Additionally, the interference effects of a compact nacelle are more sensitive to deviations in mass flow capture ratio (MFCR) from the nominal windmilling diversion condition.

Originality/value – This work provides a comprehensive analysis of not only the performance but also the aerodynamics at an aircraft level of compact nacelles compared to conventional configurations for a range of installations positions at cruise. Additionally, the engine-airframe integration aerodynamics is assessed at an off-design windmilling condition which constitutes a key novelty of this paper.

Keywords: nacelle, aerodynamics, engine-airframe integration, interference effects, computational fluid dynamics, windmilling.

I. Introduction

The reduction of the aero-engine specific fuel consumption (SFC) through an improvement of the propulsive efficiency can be achieved by higher bypass ratios (BPR) (Daly, 2010). However, this may result in a larger fan diameter that increases the overall contribution to the aircraft drag and weight and the interference effects with the airframe which can offset the engine cycle benefits (Daggett *et al*., 2003). Additionally, the installed nacelle aerodynamic characteristics can be substantially different from the isolated configuration due to the interference with the airframe (Daggett *et al*., 2003). As future engine developments are likely to adopt larger fan diameters to increase the BPR and improve SFC, structural considerations or ground clearance may force the aero-engine to be installed in a more close-coupled position with the airframe. Therefore, the aerodynamic challenge is to install larger engines with a minimal increase in drag. In this respect, Stankowski *et al*. (2016) investigated the installation effects for large civil underwing engines at Mach = 0.82 using conventional through flow nacelles (TFN) ($L_{nac}/r_{hi} = 4.3$). An increase in the installed drag from 27dc to 36dc was reported for a 23% larger engine with a geometrically scaled nacelle, which corresponds to approximately 3.5% of the standard net thrust. This increase in the installed drag can potentially be mitigated for UHBPR aero-engines by the design of more compact nacelles. Tejero *et al*. (2020) evaluated the relative performance of a compact ($L_{nac}/r_{hi} = 3.1$) and a conventional ($L_{nac}/r_{hi} = 3.8$) nacelle at cruise condition for a typical installation position of current in-service architectures. A reduction in cruise fuel burn of approximately 0.95% could be achieved for the compact nacelle relative to the conventional baseline. Wiart *et al*. (2015) highlighted a notable impact of the installation position of a UHBPR engine on the overall performance. Both axial and vertical changes in the engine position relative to the wing leading edge were investigated for a transonic cruise Mach number of M = 0.82. It was concluded that a close installation position to the wing can result into a penalty of up to 2.5% in the overall aircraft drag relative to the most forward position and largest vertical offset with the wing. Sibilli *et al*. (2012) assessed the impact of a UHBPR engine installation position on the fuel-burn for a A330-type aircraft. It was concluded that the most forward horizontal position considered could reduce the mission fuel burn up to 3.7% relative to the reference installation position. Additionally, within a broader context a novel over-the-wing engine installation for civil applications, Silva *et al*. (2022) compared against the typical podded under-the-wing nacelle arrangement. The over-the-wing installation was found to require a higher angle of attack for the same aircraft lift coefficient. This results in an increase of around 20 drag counts relative to the typical under-the-wing configuration for the aircraft trimmed condition. Further fuel consumption savings can be achieved by considering the integration aerodynamic effects between the aero-engine and the airframe within the optimisation process. Tejero *et al*. (2022a) combined dimensionality reduction and a multi-fidelity technique for the installed optimisation of a compact nacelle ($L_{nac}/r_{hi} = 3.1$). An optimised nacelle was obtained with a reduction in the overall aircraft fuel consumption of 0.55% relative to a non-axisymmetric nacelle resulting from an isolated optimisation process. A global optimum for the aero-engine integration problem is achieved by the coupled optimisation of the nacelle and the airframe. Smith *et al*. (2013) combined CFD and a gradient-based method based on adjoint to maximise the aircraft lift to drag ratio (L/D). Changes in the nacelle shape, the pitch and toe installation angles, the pylon camber and the wing shape were applied and an optimised aerodynamic of the installation was obtained. Research to reduce the nacelle contribution to the overall drag has included the design of natural laminar flow (NLF) nacelles given that friction drag can account up to 60% of the overall nacelle cruise drag (Vermeersch and Bouteiller, 2014). Zhang *et al.* (2022) derived design guidelines for transonic NLF nacelles by comparative assessments of isolated and installed nacelle aerodynamics.

Studies have shown how the engine cycle benefit of larger fan aero-engines can be eroded when installed on the aircraft. This could be mitigated by the design of more compact nacelles. Motivated by this, the aim of this paper is not only to quantify the potential performance improvements but also to provide a full understanding of the underlying aerodynamic characteristics of installed compact nacelles relative to conventional architectures for a set of forward and close-coupled installation positions at the cruise operating condition. Previous studies on the design of isolated nacelles highlighted the impact of meeting off-design requirements can have on the compact nacelle design (Daggett *et al*., 2003; Tejero *et al*., 2022b; Schreiner *et al*., 2020). However, there is no previous evaluation in the open literature of the aerodynamics of compact nacelles in installed configuration under these off-design conditions. This paper provides an evaluation of the robustness of both nacelle configurations at the off-design windmilling diversion scenario which may potentially cause shock-induced flow separation close to the leading edge due to the low mass flow ratio. Swarthout *et al*. (2023) investigated the nacelle aerodynamics at windmilling massflows for high incidence end-of-runway conditions and showed a different flow separation mechanism governed by diffusion-induced boundary layer separation initiated towards the aft of the nacelle.

II. Methodology

A. Geometry definition

The nacelle geometry is parameterised using intuitive Class Shape Transformations (iCST) developed by Christie *et al*. (2019). 3D drooped and scarfed non-axisymmetric nacelles with left-right symmetry can be defined with r_{hi}, L_{nac} and r_{te} as the key parameters that control the nacelle compactness (Figure 1). In this work, a compact (L_{nac}/r_{hi} = 3.1, r_{te}/r_{hi} = 0.95) and a conventional (L_{nac}/r_{hi} = 3.6, r_{te}/r_{hi} = 0.95) nacelle designs were evaluated in installed configurations. Both designs were down selected from a RANS-based multi-objective optimization (MOO) in isolated configuration following the method developed by Tejero *et al*. (2022b). The MOO approach took into considerations not only cruise but also low MFCR conditions through regression-type of objective functions in order to ensure aerodynamic robustness of the designs to off-design operation. This design method considered margins of local flow separation for the windmilling diversion off-design condition to reject nacelles with grossly separated flow.

Using the method from Christie *et al*. (2019), both the compact and conventional nacelle designs were combined with an intake with a ratio of intake length (L_{int}) to fan diameter (D_{fan}) close to 0.5, which is representative of typical in-service intakes for long-range applications (Petter et al., 2014). The overall power-plant systems were generated with a representative separated jet exhaust (Goulos *et al*., 2016). The bypass and core nozzle pressure ratios used were around 2.2 and 1.5 respectively (Goulos *et al*., 2021). The resulting aero-engine was representative of future large turbofans of BPR greater than 15 and nominal standard net thrust (F_N) of approximately 60kN (Goulos *et al*., 2016).The aero-engine is installed in the NASA Common Research Model (CRM), which is an open-source airframe representative of a transonic civil twin-engine wide-body aircraft configuration. The CRM cruise point is defined by a cruise Mach number of M = 0.85 and a trimmed lift coefficient of C_L = 0.5 (Rivers and Dittberner, 2014). Underwing podded engines are installed with fixed pitch-up angle of 1.75° and toe-in angle of 2.25° which is based on the CRM with TFN configurations (Rivers and Dittberner, 2014). The installation spanwise location is fixed at 33.4% of the semi-span length from the fuselage mean axis (Rivers and Dittberner, 2014). The installation position of the engine in the airframe is defined from the vertical and axial offset between the nacelle top-line trailing edge and the local wing leading edge coordinates (Figure 1). Twelve podded under-wing installation positions are evaluated. The axial offset dx/C_{wing} ranges from -0.05 to 0.05 to cover both forward and overlapped positions. The vertical offset dz/C_{wing} ranges from 0.05 to 0.15 depending on dx/C_{wing} (Figure 1). A representative pylon design is used for each installation position and nacelle design (Otter, 2018).

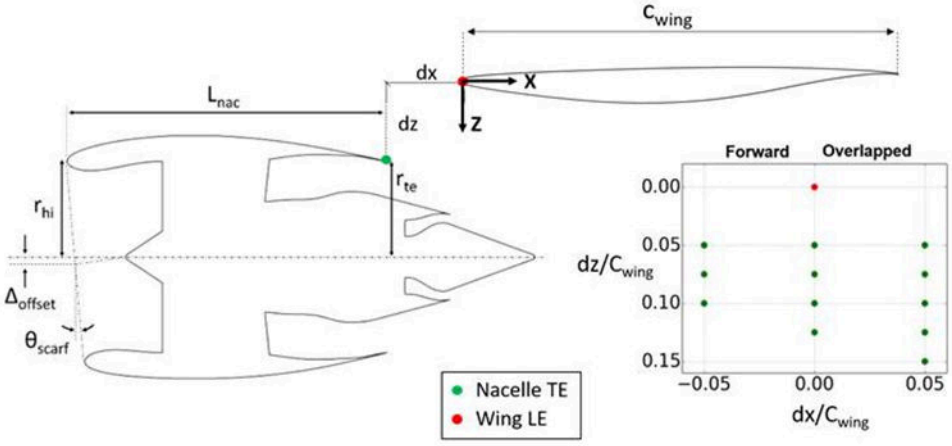

Figure 1: Key nacelle design parameters and installation positions investigated for each nacelle configuration.

B. CFD model

Half of the aircraft is considered for the CFD model based on left-right symmetry. Following the guidelines from the 4th AIAA Drag Prediction Workshop, the CFD domain is defined by a hemisphere with a radius of 100 times the

wing local chord at the installation position (Vassberg *et al*., 2014). A hybrid meshing approach is used with the first layer height adjusted to achieve a y^+ of approximately one on the wall surfaces (Vassberg *et al*., 2014). A mesh with an overall cell count of 115 million elements was selected from a grid independence study that provided a GCI of 0.48% and 1.57% for the nacelle and airframe drag respectively (Celik *et al*., 2008). A RANS solver is used to obtain a steady state, compressible flow solution. An implicit, second order upwind scheme is used for the spatial discretisation with a Green-Gauss node-based gradient interpolation method. The turbulence model used is k-ω SST (Menter, 1994). The ideal gas dynamic viscosity is calculated through Sutherland's law (Sutherland, 1893). Every solid surface on the CRM, pylon and aero-engine is modelled by a viscous wall boundary condition. The freestream static pressure (P_∞) and temperature (T_∞) and the flight Mach number (M_∞) and incidence (α) are imposed in the farfield boundary condition (Figure 2). Static pressure (P) and mass flow ($\dot{m}$) are prescribed in the intake to match the user-defined MFCR (Figure 2). The bypass and core inlets of the exhaust are modelled by the total pressure (P_0) and temperature (T_0) obtained from a 0D engine cycle analysis (Figure 2). The numerical approach was validated by Goulos *et al*. (2021) in terms of airframe drag using experimental data for the NASA CRM using TFN (Rivers and Dittberner, 2014). The installation drag is over-predicted by approximately two drag counts at cruise condition ($M = 0.85$ and $C_L = 0.5$) which is about 0.8% of the total aircraft drag. The numerical convergence was assessed by a reduction of at least five orders of magnitude in the continuity, velocity and energy residuals and four orders of magnitude in the turbulent kinetic energy and specific turbulent dissipation rate. Additionally, the aero-engine mass flow and the airframe lift and drag forces were monitored and a variation lower than 0.01% in the last 100 iterations was obtained.

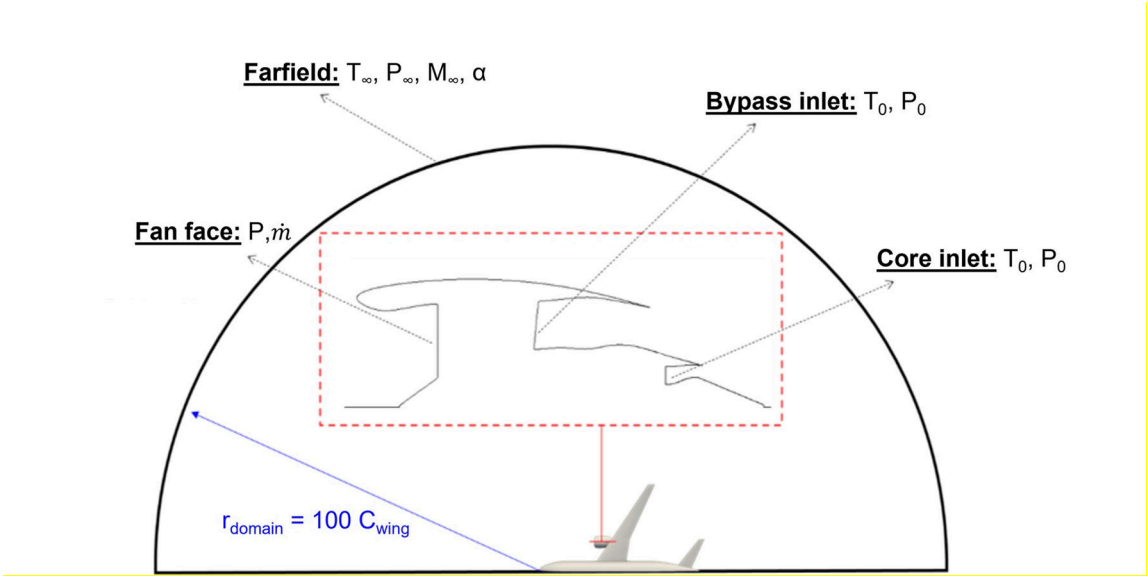

Figure 2: Schematics of the boundary conditions used in the CFD model for installed nacelle evaluations.

C. Thrust-drag accounting method

The Thrust and Drag Bookkeeping method (TDB) is based on the industrial standard practices of AGARD (1979) and extended to account for the effect of the pylon and airframe (Goulos *et al*., 2021) (Figure 3). The forces are considered positive in the downstream direction. The streamtube-external forces define the drag domain and are represented by ϕ while the streamtube-internal forces correspond to the thrust domain and are expressed by θ. The gauge stream forces across the boundaries (F_G) are calculated by integrating the pressure and momentum terms over the area of interest. The exerted forces on the engine walls are computed by integrating the pressure and viscous terms. The Net Propulsive Force (NPF) (Eq. 1) is a metric used to quantify the overall engine performance and accounts for the aerodynamic balance between the thrust and drag domains. Whereas the thrust domain is represented by the Gross Propulsive Force (GPF) (Eq. 2) the drag domain is defined by the modified nacelle drag (D^*_{nac}) (Eq. 3). Similarly, the Net Vehicle Force (NVF) (Eq. 4) reports the overall aerodynamic performance of the combined airframe and powerplant system. A detailed description of the thrust and drag accounting method is provided by Goulos *et al*. (2021).

$$NPF = GPF^* - F_{G0} - D^*_{nac} \quad (1)$$

$$\mathrm{GPF}^* = \mathrm{F_{G13}} + \mathrm{F_{G7}} - \left(\theta_{\mathrm{bp}} + \theta_{\mathrm{cc}} + \theta_{\mathrm{co}} + \theta_{\mathrm{plug}} + \theta_{\mathrm{pylon}}\right) \quad (2)$$

$$D^*_{nac} = \phi_{pre} + \phi_{nac} \quad (3)$$

$$NVF = NPF - D_{a/f} \quad (4)$$

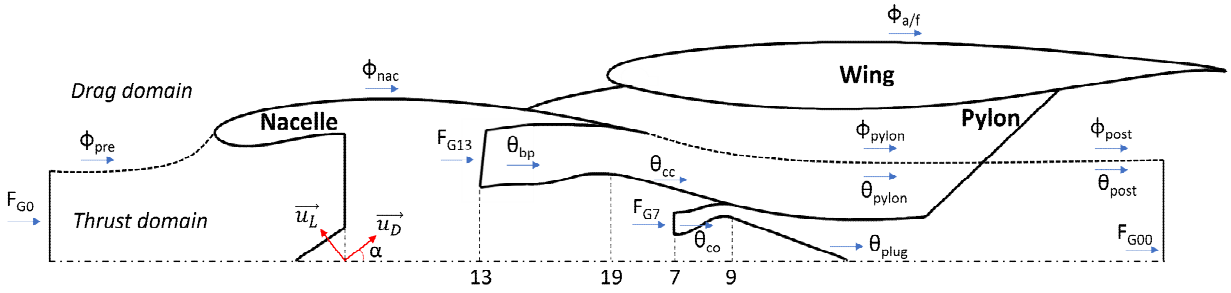

Figure 3: Thrust and drag bookkeeping method for installed aero-engine configuration.

D. Off-design nacelle evaluation

The aerodynamic robustness of the nacelle designs to off-design conditions are assessed for the windmilling diversion operating point. At this condition with a shutdown aero-engine the MFCR is significantly reduced to an expected value of around 0.3 (ESDU, 1981; Obert, 2009) which may potentially cause shock-induced flow separation close to the nacelle leading edge. Relative to the design condition, the flight velocity, altitude and the mass flow through the aero-engine are reduced. A common practice is to use M = 0.65 for this condition (Schreiner *et al*., 2020; Zachos, 2013). The C_L for this condition is re-trimmed for the changes in the altitude and flight velocity to maintain the same lift as in cruise. For this preliminary evaluation at windmilling diversion, freestream total pressure and temperature are imposed in both bypass and exhausts inlets. The plausibility of this assumption is based on the low mass flow through the aero-engine core path, the null enthalpy exchanges between components and the fan pressure ratio being close to one (Braig *et al*., 1999). The aero-engine installation position is set to $dx/C_{wing} = 0$ and $dz/C_{wing} = 0.1$ (Figure 1) for both the compact and conventional configurations.

III. Results and analysis

As shown in Section I, previous work has assessed the aerodynamics of installed compact and conventional nacelles in cruise. In this paper, the cruise evaluation in Section III.E is included to provide a more in-depth assessment of the changes in pressure drag force on the nacelle and wing for forward and close-coupled installation positions as well as providing context for the subsequent off-design assessments in Section III.F.

E. Analysis at mid-cruise condition

The CRM mid-cruise condition (M = 0.85 and $C_L = 0.5$) is considered for this analysis (Rivers and Dittberner, 2014). A MFCR = 0.7 is estimated for mid-cruise from engine deck datasets (Goulos *et al*., 2021). The impact of installation on the nacelle aerodynamic is highly influenced by both the installation position and the powerplant compactness. For the compact nacelle ($L_{nac}/r_{hi} = 3.1$) the effect of the installation position on the overall NVF is a balance between the sensitivities of its constituent metrics (NPF, $D_{a/f}$ and D^*_{nac}) (Figure 4). The variation of each metric across the installation map is reported as a percentage of the reference standard net thrust (F_N = 60kN) and relative to the lowest value of the metric. The maps provide an individual range of sensitivity to installation position. NPF and D^*_{nac} are primarily affected by the axial installation position with the region of highest benefit located at the most forward position ($dx/C_{wing} = -0.05$) (Figure 4b, Figure 4c). Conversely, $D_{a/f}$ and NVF depend on both the axial and vertical coordinates (Figure 4a, Figure 4d). The regions of highest benefit of each metric are placed at the largest vertical offset from the wing leading edge but opposed directions in terms of the axial coordinate. While the greatest NVF is located at the most forward installation position ($dx/C_{wing} = -0.05$, $dz/C_{wing} = 0.1$), the lowest $D_{a/f}$ is at the most overlapped position ($dx/C_{wing} = 0.05$, $dz/C_{wing} = 0.15$). The same trend in distributions of all the metrics across the installation map is observed for the conventional nacelle design ($L_{nac}/r_{hi} = 3.6$) albeit with different levels.

While the variation in the NVF in the installation design space for the compact design is $0.053F_N$ (Figure 4d), it is $0.039F_N$ for the conventional nacelle. These variations highlight the greater sensitivity of the compact configuration to the installation.

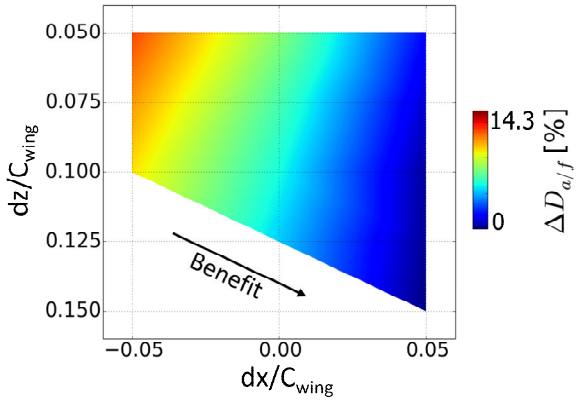

a) Compact nacelle, airframe drag ($D_{a/f}$)

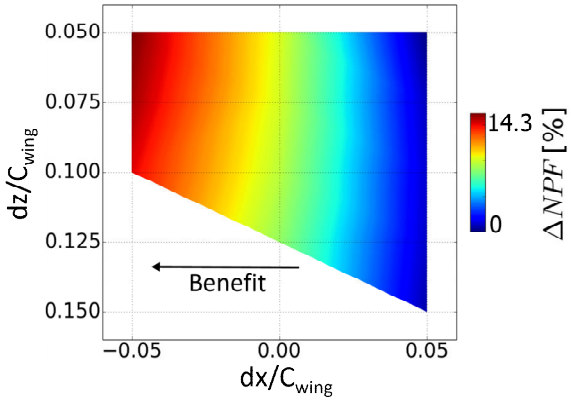

b) Compact nacelle, Net Propulsive Force (NPF)

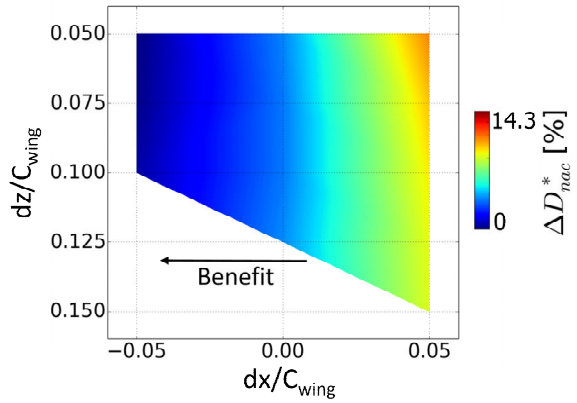

c) Compact nacelle, modified nacelle drag (D^*_{nac})

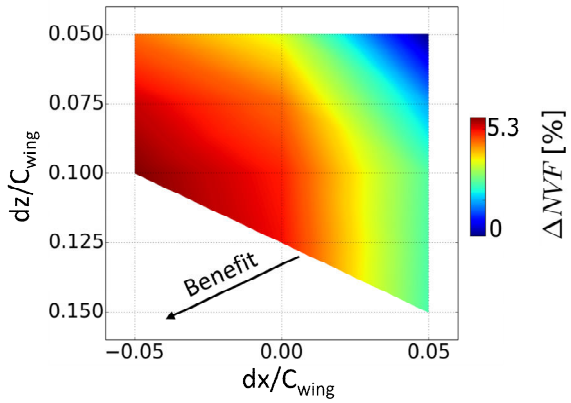

d) Compact nacelle, Net Vehicle Force (NVF)

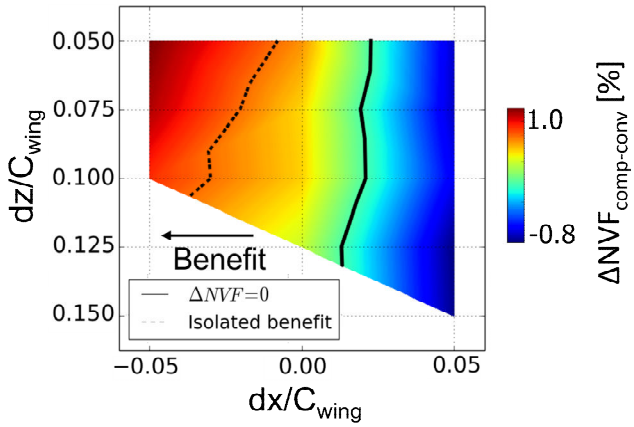

e) Net Vehicle Force benefit ($\Delta NVF_{comp\text{-}conv}$) of the compact relative to the conventional configuration

Figure 4: Installation maps at the cruise condition.

The distribution of the NVF benefit of the compact architecture relative to the conventional one $\Delta NVF_{comp\text{-}conv} = 100\ (NVF_{compact} - NVF_{conventional})/F_N$ is broadly dominated by the axial installation position (Figure 4e). The

maximum $\Delta NVF_{comp\text{-}conv}$ reaches 1% and it is located at the most forward installation position, dx/C_{wing} = -0.05 and dz/C_{wing} = 0.05. At $dx/C_{wing} \sim 0.025$ there is a change in the polarity of $\Delta NVF_{comp\text{-}conv}$. The compact nacelle has a NVF penalty relative to the conventional design at close-coupled installation positions. It reaches up to -0.8% for dx/C_{wing} = 0.05. This is a challenging outcome as compact nacelles for UHBPR aero-engines may be installed in a more close-coupled installation position due to the multi-disciplinary constraints such as ground clearance or structural considerations. For a conventional installation position (dx/C_{wing} = 0 and dz/C_{wing} = 0.1), the compact nacelle benefit is $\Delta NVF_{comp\text{-}conv} \sim 0.44\%$. This equates to an aircraft cruise fuel burn reduction of the same order. In comparison, the expected benefit for the compact nacelle in the isolated configuration was ~0.7%. This highlights the need to consider the integration effects throughout the nacelle design phase when the aero-engine is installed in closer positions to the airframe.

The aerodynamics of the combined system has been investigated through distributions of elemental pressure force in the drag direction $\left(\frac{1}{q_\infty}\frac{dF_p}{dS}\Big|_D\right)$ on the nacelle surface and the wing pressure side. The conventional installation position (dx/C_{wing} = 0 and dz/C_{wing} = 0.1) is used as a reference. On the nacelle, the largest contribution to the drag is located in the inboard afterbody region due to the high flow suction that arises from the interference with the airframe and pylon (Figure 5). Conversely, the flow suction in the nacelle forebody provides a drag benefit. On the wing pressure side the interference flow with the nacelle generates a force in the thrust direction that reduces the drag of the overall system.

The compact nacelle configuration is used to explore the impact of the installation position on the aerodynamics of the propulsion system integration (Figure 5). A comparison between dz/C_{wing} = 0.075 and 0.125 at fixed dx/C_{wing} = 0 shows the impact of the vertical installation position. As stated before, there is a low influence of the vertical coordinate on the nacelle drag. Slight changes in the shock intensity arise in the rear inboard region of the nacelle. Overall, D^*_{nac} increases by $0.003F_N$ for dz/C_{wing} = 0.125 relative to dz/C_{wing} = 0.075. Conversely, there is a bigger impact of the vertical installation position on the airframe drag. In the inboard forebody region of the wing, the intensity of the flow suction is greater for dz/C_{wing} = 0.125 which reduces $D_{a/f}$ by $0.016F_N$ relative to dz/C_{wing} = 0.075. Overall, dz/C_{wing} = 0.125 has a $\Delta NVF_{comp\text{-}conv}$ of 0.5% over dz/C_{wing} = 0.075. Similarly, the impact of the horizontal installation position is explored through the axial positions given by dx/C_{wing} = -0.05 and 0.05 at fixed dz/C_{wing} = 0.1. In this case, the sensitivity of the changes in the airframe and nacelle aerodynamics are of the same order of magnitude. For the close-coupled position (dx/C_{wing} = 0.05) the flow suction in the inboard side of the nacelle afterbody and wing forebody is substantially increased in magnitude and area compared to dx/C_{wing} = -0.05. Therefore, dx/C_{wing} = 0.05 presents a $0.090F_N$ increase in D^*_{nac} and a $0.092\ F_N$ reduction in $D_{a/f}$ relative to dx/C_{wing} = -0.05. Overall, the most forward installation position dx/C_{wing} = -0.05 reaches a $\Delta NVF_{comp\text{-}conv}$ of 2.9% which emphasises the stronger sensitivity to the axial installation position compared to the vertical position.

Similar changes in the distributions of elemental pressure drag force with the horizontal installation position are observed for the compact and conventional nacelle configurations (Figure 5, Figure 6). However, there are changes in the magnitude of this elemental pressure drag between both nacelles. This is shown through transversal cuts along different circumferential location in the nacelle (Φ = 0º (top), 45º, 90º, 135º and 180º, Figure 7a) and different axial wing span sections ($\eta = y/b_{wing}$ = 0.15, 0.20, 0.25 and 0.3, Figure 7b) on the inboard side. There is a smaller region of high flow suction on the inboard side of the nacelle and wing for the conventional nacelle installation. This occurs for both the forward and close-coupled positions (Figure 7). The largest change on the nacelle is located on the upper half inboard side between Φ = 45º and 90º (Figure 7). On the inboard side of the wing the pressure drag force change increases closer to the pylon (Figure 7). Relative to the compact configuration, a slightly weaker shock wave arises in the inboard nacelle and wing at both installation positions. For dx/C_{wing} = -0.05, the D^*_{nac} is reduced by $0.089F_N$ while the $D_{a/f}$ is increased by $0.100F_N$ relative to dx/C_{wing} = 0.05. Overall, the $\Delta NVF_{comp\text{-}conv}$ of the forward position dx/C_{wing} = -0.05 relative to dx/C_{wing} = 0.05 reaches 1.5%, which is half of the benefit achieved for the compact nacelle configuration. This highlights the higher sensitivity of the compact nacelle to a close-coupled installation.

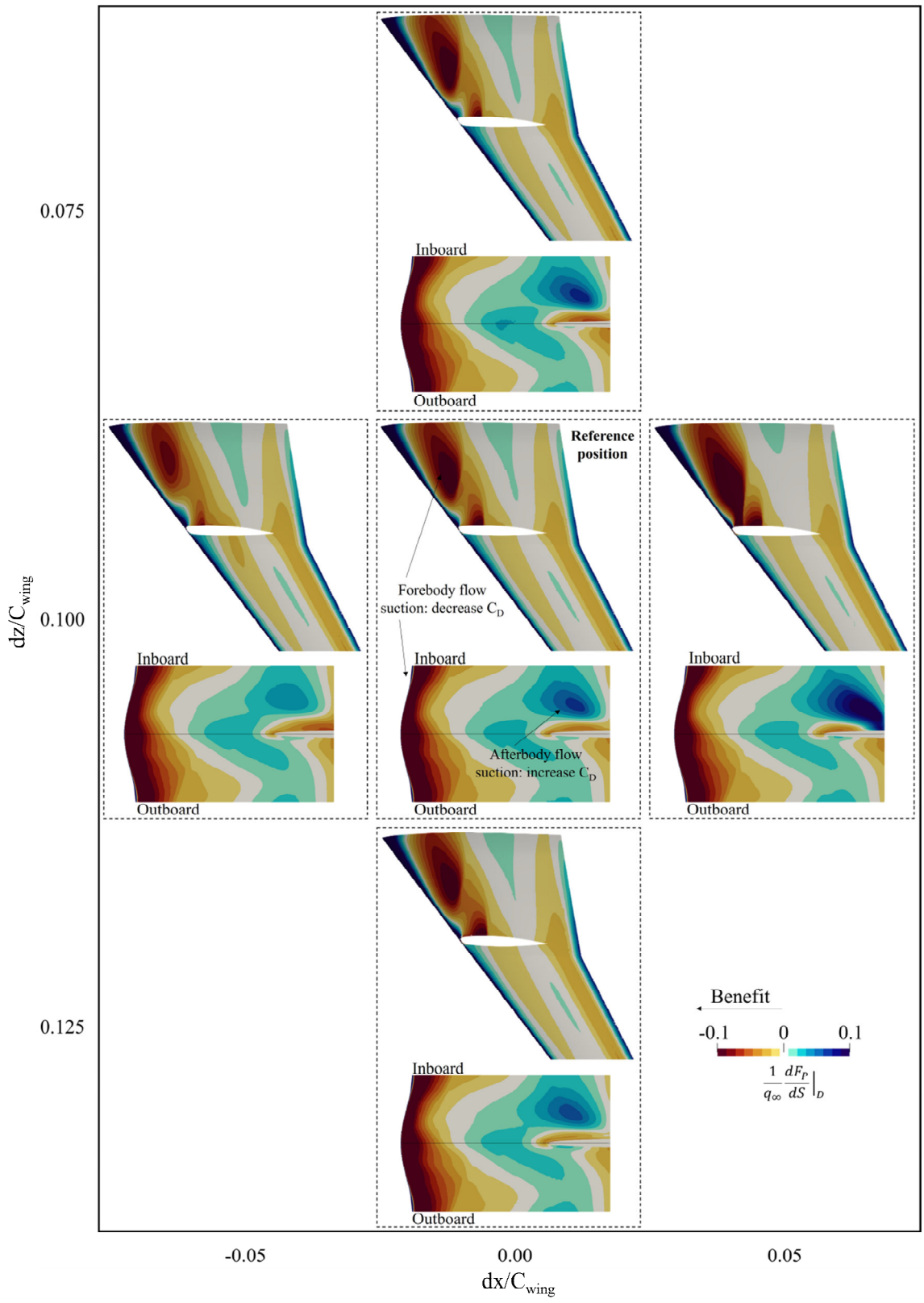

Figure 5: Contours of elemental pressure force in the drag direction for the cruise trim condition (C_L = 0.5) at a range of installation positions. Pressure side of the wing and unwrapped nacelle. Compact configuration.

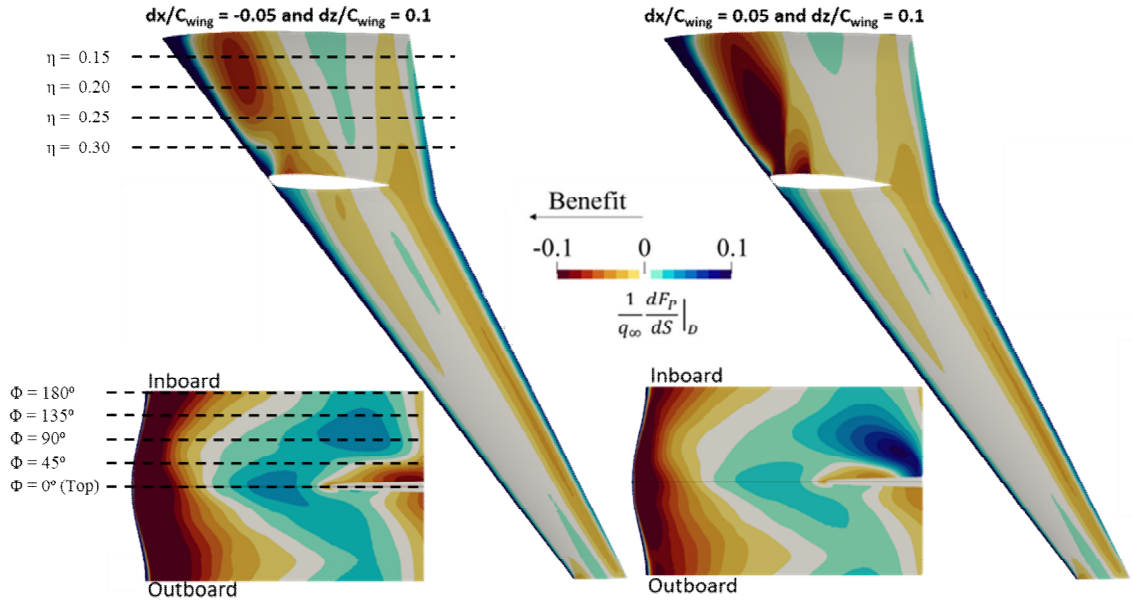

Figure 6: Contours of elemental pressure force in the drag direction for the cruise trim condition (C_L = 0.5). Pressure side of the wing and unwrapped nacelle. Conventional configuration. Impact of the horizontal installation position. **(figure by authors)**

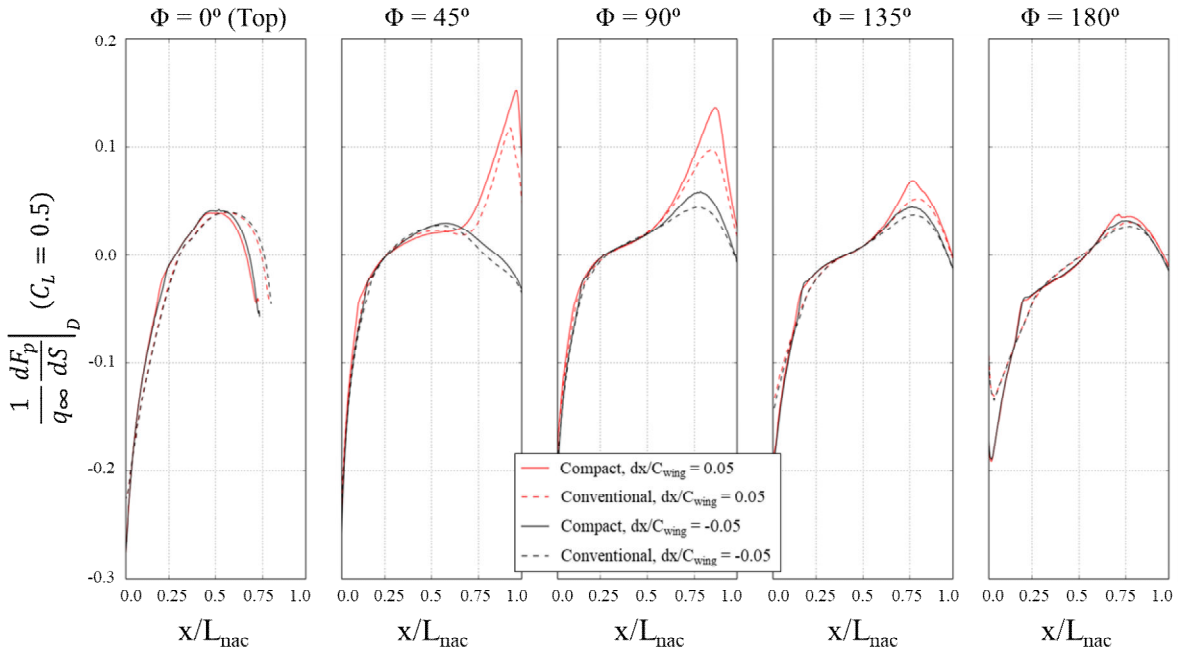

a) Circumferential cuts along the nacelles: Φ = 0º (top), 45º, 90º, 135º and 180º.

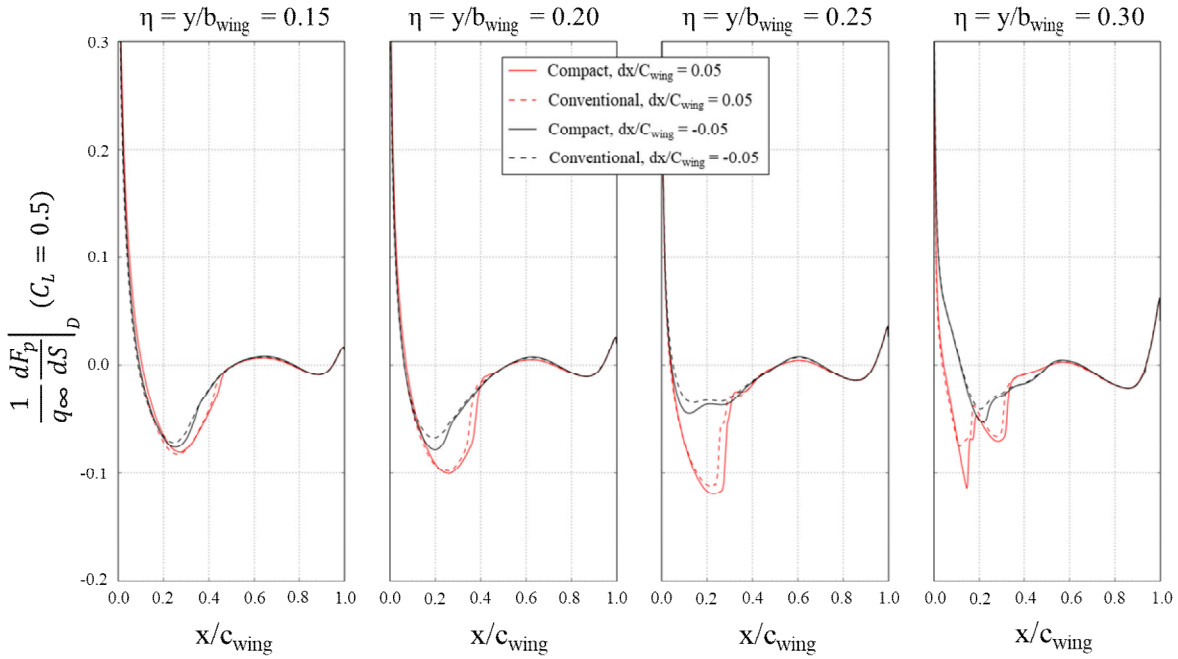

b) Axial cuts along the wing span: $\eta = y/b_{wing} = 0.15$, 0.20, 0.25 and 0.3.

Figure 7: Distribution of elemental pressure force in the drag direction for the cruise trim condition ($C_L = 0.5$) along different cuts of the nacelle and pressure side of the wing. Compact and conventional nacelle configuration. Impact of the horizontal installation position at $dz/C_{wing} = 0.1$.

F. Analysis at windmilling diversion condition

For the reference installation position ($dx/C_{wing} = 0$ and $dz/C_{wing} = 0.1$), there is a NVF penalty at windmilling diversion of $\Delta NVF_{comp\text{-}conv} = -2.6\%$ for the compact nacelle relative to the conventional one (Figure 9a). This highlights the higher sensitivity of the performance of the compact nacelle design to this off-design condition. From an aerodynamic standpoint, windmilling diversion is normally governed by shock-induced flow separation close to the highlight of the nacelle. The high curvature gradients on the geometry of the compact nacelle trigger a larger extent of flow separation relative to the conventional configuration (Figure 8a, Figure 8b). The separation in the inboard region of the compact nacelle is slightly amplified compared to the outboard part due to the crossflow induced by the interaction with the airframe and pylon and also because of the toe installation angle (Figure 8a). However, there are not notable differences in the overall extent of flow separation between the isolated and installed configurations apart from the fact that the separated region is symmetric for the isolated case (Figure 8a, Figure 8c). This highlights the little impact of the aero-engine installation on the flow separation for windmilling diversion for both the compact and the conventional configurations. The spillage flow in the leading edge of the nacelle caused by the low engine mass flow governs the flow separation at this off-design condition.

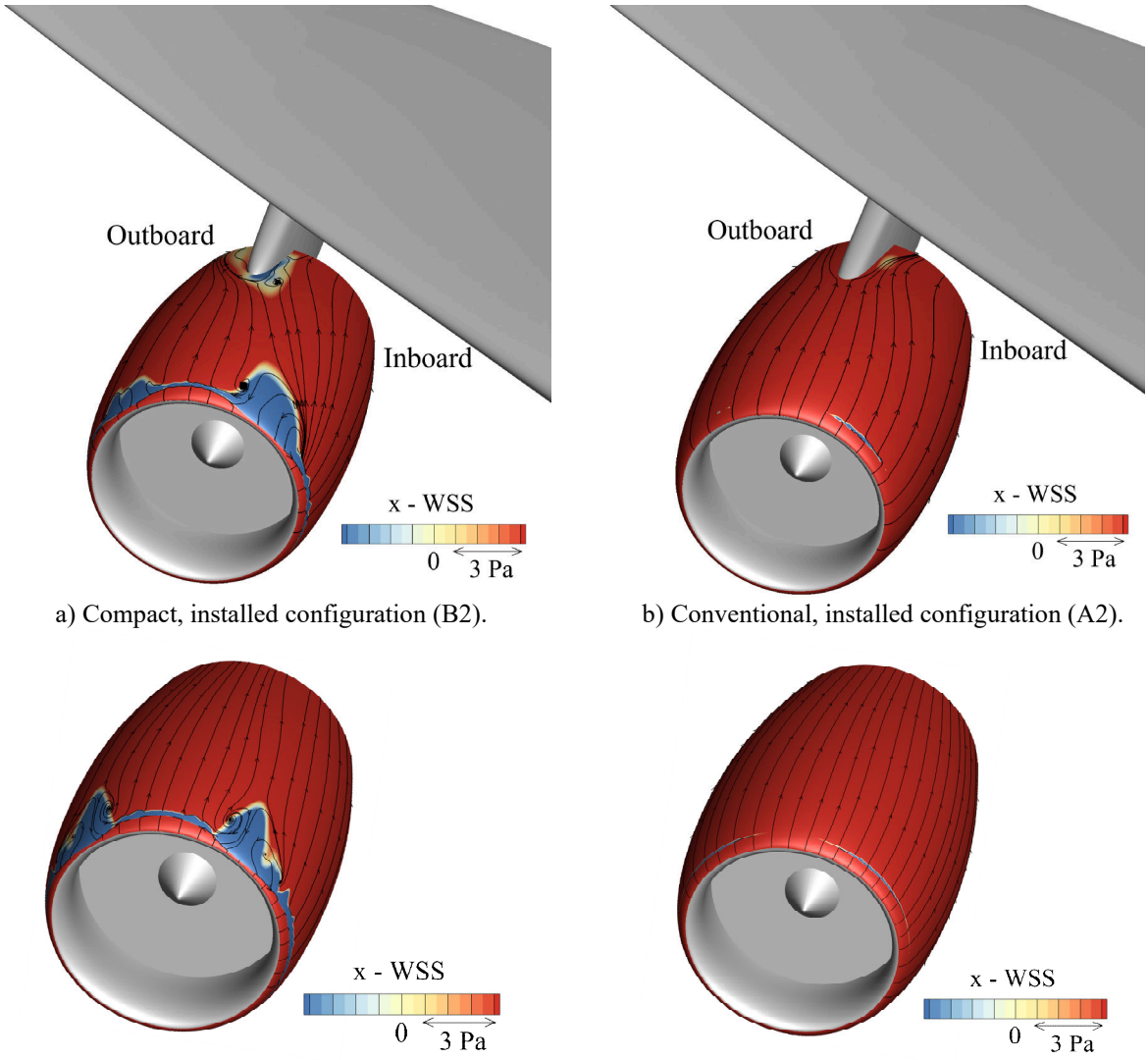

a) Compact, installed configuration (B2).

b) Conventional, installed configuration (A2).

c) Compact, isolated configuration.

d) Conventional, isolated configuration.

Figure 8: Contours of x-component of the wall shear stress and surface streak-lines for the nominal windmilling diversion operating condition. Compact and conventional nacelle designs. Installed trimmed configuration at $dx/C_{wing} = 0.0$ and $dz/C_{wing} = 0.1$ and isolated configuration.

A key parameter at windmilling diversion-type of conditions is the aero-engine MFCR. The MFCR affects the location of the stagnation point in the intake and consequently the flow suction around the nacelle leading edge. The sensitivity of both the compact and conventional nacelles to changes in MFCR is evaluated in the airframe-installed configuration. The bounds of the investigated range of MFCR depended on the nacelle design (Figure 9). For the conventional nacelle the MFCR was varied by about +/- 0.05 relative to the nominal windmilling diversion condition (A2) to encompass both attached and separated (A3) cases. For the compact configuration at the nominal MFCR condition (B2) the flow was already fully separated. The MFCR was increased by about 0.17 to the case at which the nacelle flow was predominantly attached (B5).

For low values of MFCR, the installed performance of the compact nacelle based on NVF is more sensitive to changes in MFCR. For example, a decrease in MFCR of 0.05 reduces the NVF of the installation relative to the NVF of the clean CRM airframe $\Delta NVF_{installation} = {}^{100\ (NVF_{Installed} - NVF_{CleanCRM})}/_{D_{Aircraft}}$ by 1% and 3% for the conventional and compact nacelle designs respectively (Figure 9a). For the same variation in MFCR, the change in D^*_{nac} for the conventional and compact nacelle is about by 0.5% and 2% of the total aircraft drag respectively (Figure 9b). For both the conventional and compact nacelle designs, the airframe drag component is broadly

unaffected by the variation in the MFCR. This is sensible since MFCR is a parameter that at windmilling diversion essentially affects the forebody of the nacelle with little impact on the installation. Overall the $D_{a/f}$ increases slightly by about 0.3% across the range of MFCR studied (Figure 9c). This shows that the different sensitivities in $\Delta NVF_{installation}$ are governed by the nacelle drag. Moreover, the large sensitivity of the compact nacelle to the changes in MFCR strongly highlights the importance of a proper estimation of the MFCR for this off-design operating condition for compact nacelle configurations.

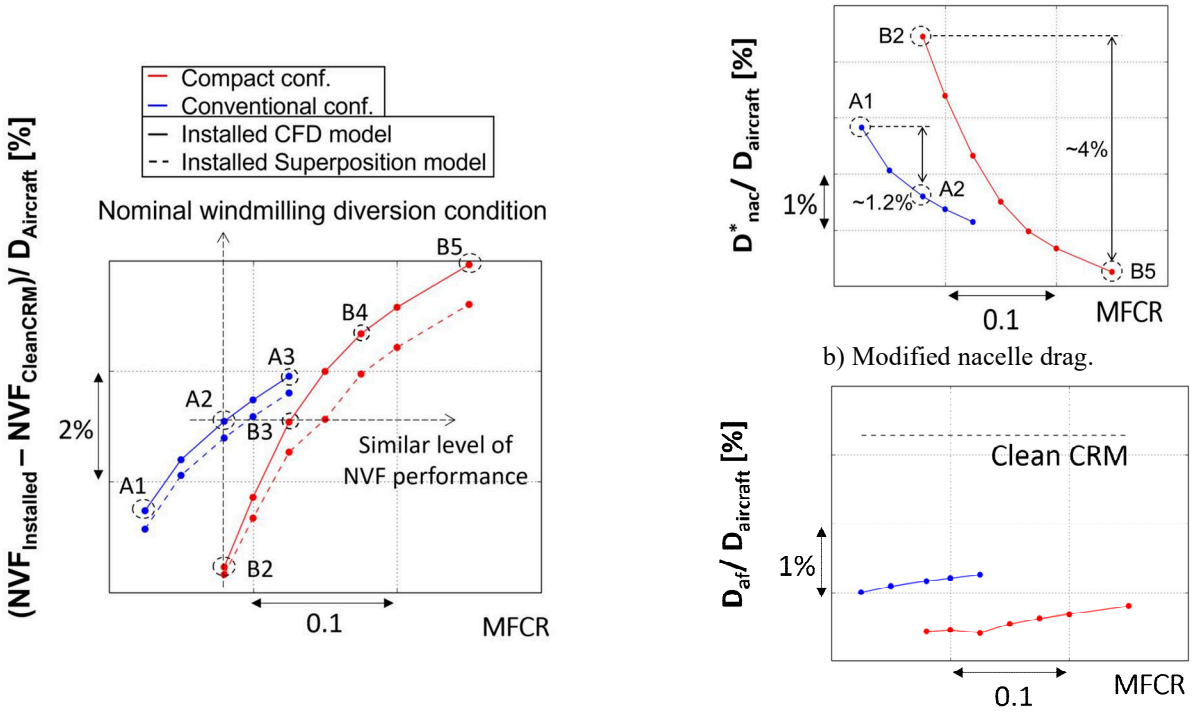

a) Net vehicle force.

b) Modified nacelle drag.

c) Airframe drag.

Figure 9: Sensitivity of installation to MFCR for windmilling diversion-type of conditions for the compact and conventional nacelle designs. Installed CFD and superposition models. Installed trimmed configuration at dx/C_{wing} = 0.0 and dz/C_{wing} = 0.1.

From the distributions of the separated flow (Figure 8) it has been shown that the $\Phi = 45^o$ aeroline is the most significant for windmilling diversion. Therefore, the isentropic Mach number distributions on this aeroline at $\Phi = 45^o$ are used to show the sensitivity of both nacelles to variations in MFCR (Figure 10). This encompasses the separated cases (Conventional - A1, Compact - B2, B3, B4) as well as predominantly attached conditions (Conventional – A2, A3, Compact – B5). For the compact nacelle conditions B3 and B4 are between the fully separated (B2) and attached (B3) cases (Figure 9a). In addition, for the conventional nacelle the conditions include A1 which is fully separated and also A2 and A3 which are broadly attached (Figure 9a). A typical isentropic Mach number (M_{is}) distribution for a separated boundary layer for this windmilling diversion-type condition shows a strong flow acceleration and shock wave around the highlight with a peaky M_{is} distribution. The comparison between compact and conventional nacelles shows how, for the complete range of MFCR evaluated for the conventional configuration, the compact design is fully separated (Figure 10). For the conventional nacelle as the MFCR is reduced by about 0.05 from A3 to A2 there is an increase in the peak M_{is} which gives rise to a small local separation but the flow remains predominantly attached (Figure 10a). An additional reduction in the MFCR by about 0.05 results in great acceleration at the nacelle leading edge and a further increase in the peak M_{is} which gives rise to separation (Figure 10a). Broadly similar characteristics are noted for the compact nacelle. As the MFCR is reduced by 0.075 from the relatively high MFCR at B5 with attached flow to B4 there is similarly a notable increase in peak M_{is} (Figure 10b). Although the flow is not fully separated, the increase in the peak M_{is} gives rise to a medium size separated flow bubble. A further reduction in MFCR on B3 and B2 ultimately results in a more notable separated

region with a fully separated flow topology (Figure 10b). After around x/L_{nac} = 0.20 and 0.30 for the conventional and compact nacelles respectively the M_{is} is barely affected by MFCR (Figure 10). All of this highlights the critical importance of the nacelle leading edge design due to the notable sensitivity to modest changes in MFCR.

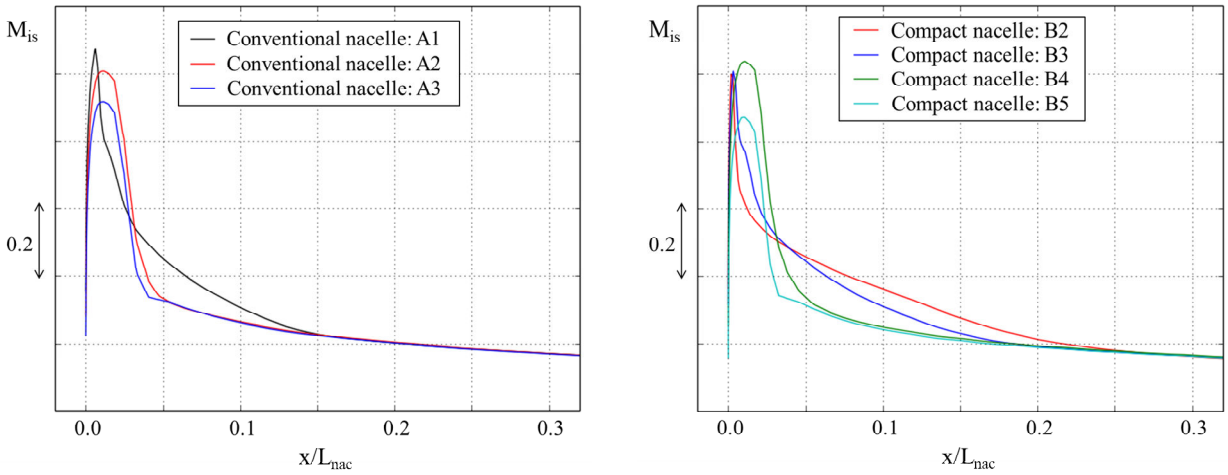

a) Conventional nacelle b) Compact nacelle

Figure 10: Distribution of isentropic Mach number (Mis) along the forebody (until 0.3Lnac) of the compact and conventional nacelle configurations at the $\Phi = 45^{o}$ aeroline for windmilling-type of conditions at different MFCR. Installed trimmed configuration at dx/C_{wing} = 0.0 and dz/C_{wing} = 0.1.

To assess the relationship between the nacelle drag and the changes in flow distribution in more details, a comparison of the M_{is} distributions (Figure 12) and contours of elemental pressure drag distribution (Figure 11) for both nacelles are considered. This includes conditions of generally attached flow (A2 and B5) and grossly separated flow (A1 and B2). There is a modest effect of the installation in the inboard part of the rear nacelle that increases the elemental drag due to the flow suction induced by the interference with the pylon and wing but this is only slightly affected by the MFCR (Figure 11, Figure 12). The axial changes in this elemental drag force around the crest and the afterbody of the nacelle are modest compared to the region near the leading edge (Figure 11). This general distribution applies regardless of the nacelle compactness and flow separation. For the cases with separated flow, which are evident in the distributions of x-component of wall shear stress at $\Phi = 45^{o}$ (Figure 13), the signature of the separated flow is close to the leading edge both in the contours of pressure drag force (Figure 11) and in the M_{is} distributions (Figure 12). As a consequence of the flow separation, the suction near the leading edge is reduced and the drag increases substantially (Figure 11). For example, for the compact configuration, D^{*}_{nac} increases by around 4% of the aircraft drag at diversion from the fully attached flow case (B5) to the grossly separated case at the nominal diversion scenario (B2) (Figure 9b).

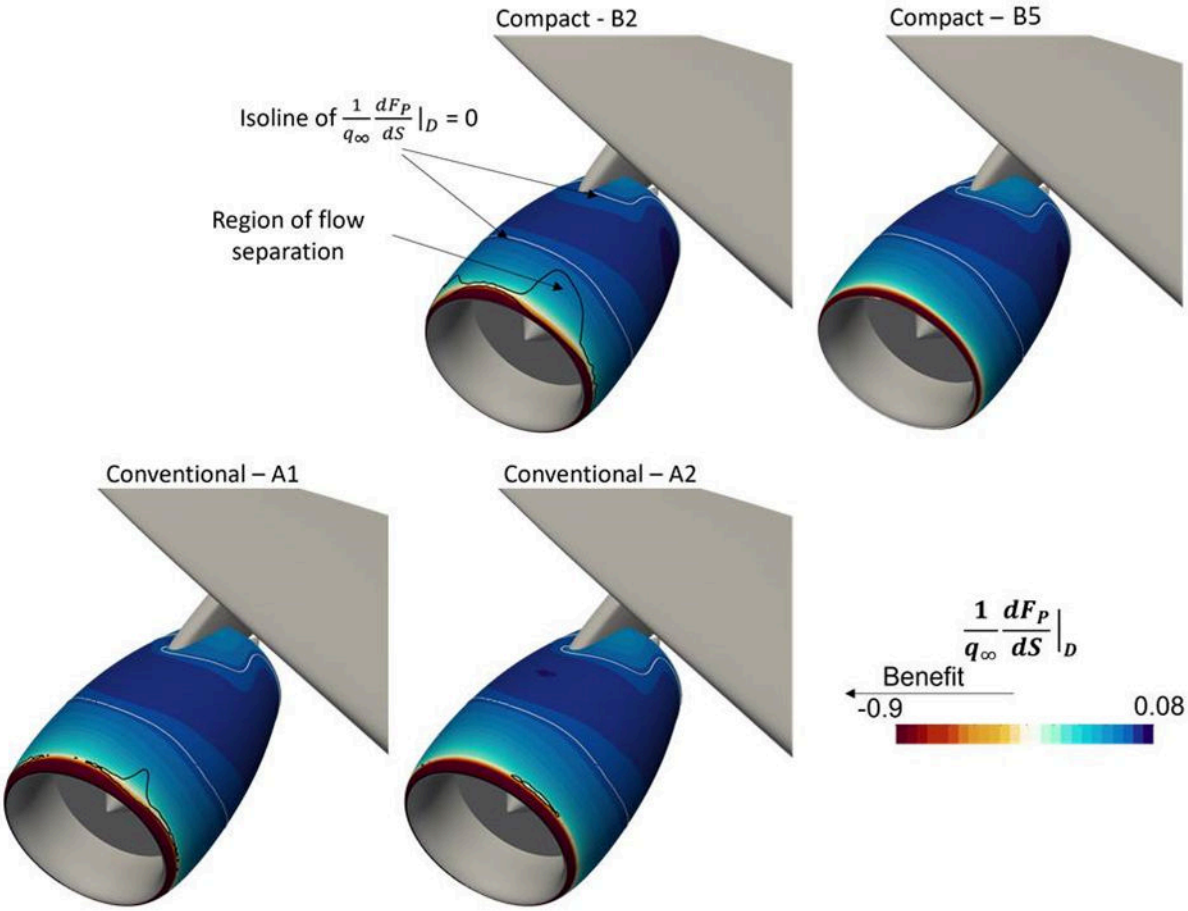

Figure 11: Contours of elemental pressure drag force for the compact and conventional nacelle configuration for windmilling-type of conditions at different MFCR. The black line indicates x-component of wall shear stress equal to 0 as an approximate indication of the separated flow regions. Installed trimmed configuration at $dx/C_{wing} = 0.0$ and $dz/C_{wing} = 0.1$.

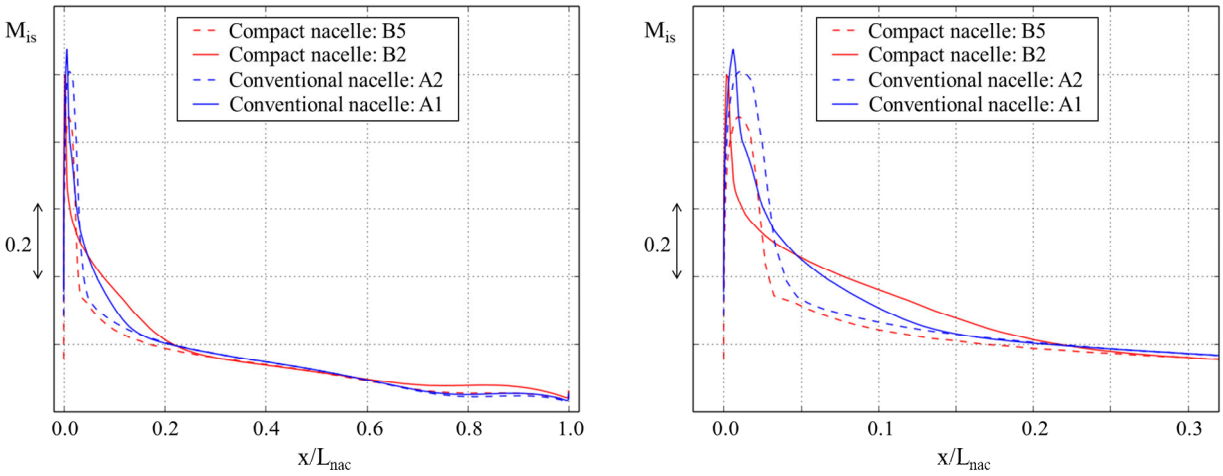

a) M_{is} along the complete nacelle aeroline. b) M_{is} along the forebody (until $0.3L_{nac}$).

Figure 12: Distribution of isentropic Mach number (M_{is}) for the compact and conventional nacelle configurations at $\Phi = 45^{o}$ for windmilling-type of conditions at different MFCR showing separated (A1 and B2) and attached (A2 and B5) conditions. Installed trimmed configuration at $dx/C_{wing} = 0.0$ and $dz/C_{wing} = 0.1$.

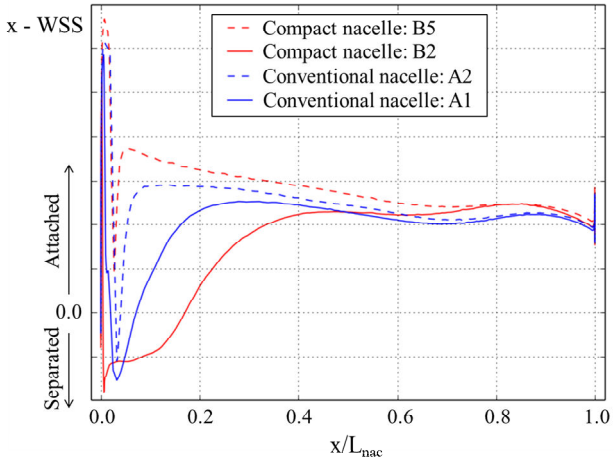

Figure 13: Distribution of x-component of the wall shear stress for the compact and conventional nacelle configurations at $\Phi = 45^{o}$ for windmilling-type of conditions at different MFCR for attached and separated conditions. Installed trimmed configuration at $dx/C_{wing} = 0.0$ and $dz/C_{wing} = 0.1$.

Finally, the installation effects for each nacelle configuration at these windmilling diversion-type of conditions have been quantified with the use of a superposition model. This superposition model provides the NVF_{Sup} by the balance between the aero-engine thrust in the installed operation condition ($T_{installed}$) and the individual drag components of the nacelle ($D_{nac,isolated}$) and airframe ($D_{CleanCRM}$) evaluated in isolation (Eq. 5). For the nominal diversion condition, the interference effects are approximately 0.2% and 0.4% for the compact and conventional nacelle respectively (Figure 9a). While this interference effects are approximately constant with MFCR for the conventional nacelle design, they increase with MFCR for the compact configuration. In particular, for the attached flow condition (B5), the interference effects account for approximately 0.7% of the overall aircraft drag. Additionally, for a similar level of NVF performance between the compact and the conventional designs (A2 and

B2), the interference effects for the compact configuration increases by a factor of 3 compared to the conventional configuration. This highlights the need to perform installed nacelle design for compact nacelle architectures.

$$NVF_{Sup} = T_{installed} - D_{nac,isolated} - D_{CleanCRM} \quad (5)$$

IV. Conclusions

This work has investigated the aerodynamic effects of integration in future civil aero-engines. The sensitivity to key parameters such as the vertical and axial installation positions have been considered. The changes in the aerodynamics on the nacelle and the airframe were analysed to provide a better insight of the associated flow physics. For this purpose, a 3D non-axisymmetric compact (L_{nac}/r_{hi} = 3.1) and conventional (L_{nac}/r_{hi} = 3.6) nacelle designs were down selected from a multi-objective optimisation in isolated configuration and have been installed in the CRM aircraft. The analysis of the integration and interference effects of the aero-engine with the airframe has shown substantial aerodynamic deviations from the isolated behaviour for close-coupled installation positions, especially in the inboard side of the nacelle. Therefore, it has been concluded the need to account for the integration effects throughout the nacelle design process for the next generation of UHBPR aero-engines which may be installed in a more close-coupled position. A well-established thrust-drag bookkeeping method has been applied to evaluate the overall performance of the installed powerplant in terms of not only the NVF but also its constituent metrics: net propulsive force, airframe drag and modified nacelle drag. Different installation positions have been evaluated for both nacelle configurations at cruise operating condition. The NVF benefit of the compact powerplant relative to the conventional architecture is primarily affected by the axial installation position, ranging from $0.01F_N$ benefit at forward installation positions to $-0.008F_N$ penalty at very closed-coupled positions. At the reference installation position (dx/C_{wing} = 0 and dz/C_{wing} = 0.1), the NVF benefit of the compact design is $0.004F_N$ which equates to an aircraft cruise fuel burn reduction of the same order. To get an estimate of the nacelle designs robustness at off-design conditions, both nacelle configurations have been evaluated for windmilling diversion-type operating conditions at the reference installation position. At the nominal windmilling diversion condition, the compact design exhibits a large flow separation that is translated into a NVF penalty of approximately $-0.026F_N$ relative to the conventional design. Additionally, the compact architecture is more sensitive to deviations in MFCR from the nominal windmilling diversion condition. The interference effects estimated from a superposition model are also more sensitive to changes in MFCR for the compact nacelle configuration. This highlights the importance of a proper estimation of the MFCR for this off-design operating conditions for compact nacelles.

References

Braig, W., Schulte, H. and Riegler, C. (1999), "Comparative analysis of the windmilling performance of turbojet and tbrbofan engines", *Journal of Propulsion and Power*, Vol. 15 No. 2, pp. 326-333, doi: 10.2514/2.5430.

Celik, I. B., Ghia, U., Roache, P. J. and Freitas, C. J. (2008), "Procedure for estimation and reporting of uncertainty due to discretization in CFD applications", *Journal of Fluids Engineering,* Vol. 130 No. 7, pp. 780011–780014, doi: 10.1115/1.2960953.

Christie, R., Robinson, M., Tejero, F. and MacManus, D. G. (2019), "The use of hybrid intuitive class shape transformation curves in aerodynamic design", *Aerospace Science and Technology*, Vol. 95, doi: 10.1016/j.ast.2019.105473.

Daggett, D. L., Brown, S. T. and Kawai, R. T. (2003), "Ultra-efficient engine diameter study", NASA-CR-2003-212309.

Daly, M. (2010), *Jane's aero-engines*, IHS Global Ltd.

ESDU (1981), "Estimation of windmilling drag and airflow of turbo-jet and turbo-fan engines", ESDU-81009, Engineering Sciences Data Unit.

Goulos, I., Stankowski, T., Otter, J., MacManus, D., Grech, N. and Sheaf, C. (2016), "Aerodynamic design of separate-jet exhausts for future civil aero-engines—Part I: Parametric geometry definition and computational fluid dynamics approach", *Journal of Engineering for Gas Turbines and Power*, Vol. 138 No. 8, doi: 10.1115/1.4032649.

Goulos, I., Otter, J., Tejero, F., Rebassa, J. H., MacManus, D. and Sheaf, C. (2021), "Civil turbofan propulsion aerodynamics: Thrust-drag accounting and impact of engine installation position", *Aerospace Science and Technology*, Vol. 111, doi: 10.1016/j.ast.2021.106533.

Menter, F. R. (1994), "Two-equation eddy-viscosity turbulence models for engineering applications", *AIAA Journal*, Vol. 32 No. 8, pp. 1598-1605, doi: 10.2514/3.12149.

Ministry-Industry Drag Analysis Panel. (1979), "Study Group. Guide to in-flight thrust measurement of turbojets and fan engines", AGARD-AG-237, MIDAP.

Obert, E (2009), *Aerodynamic design of transport aircraft*, IOS Press.

Otter, J. J. (2018), "Aerodynamics and performance of civil aero-engine exhaust systems", PhD Thesis, Cranfield University, https://dspace.lib.cranfield.ac.uk/handle/1826/13299.

Peters, A., Zoltan, S. S., Wesley, K. L. and Becky, R. (2014), "Ultra-short nacelles for low fan pressure ratio propulsors", *Volume 1A: Aircraft Engine; Fans and Blowers*, doi: 10.1115/GT2014-26369.

Rivers, M. B. and Dittberner, A. (2014), "Experimental investigations of the NASA common research model", *Journal of Aircraft*, Vol. 51 No. 4, pp. 1183-1193, doi: 10.2514/1.C032626.

Schreiner, B. D. J., Tejero, F., MacManus, D. G. and Sheaf, C. (2020), "Robust aerodynamic design of nacelles for future civil aero-engines", Proceedings of ASME Turbo Expo, virtual, GT2020-14470.

Sibilli, T., Savill, M., Sethi, V., MacManus, D. and Rolt, A. M. (2012), "Numerical simulation of propulsion system integration for very high bypass ratio engines", Proceedings of ASME Turbo Expo, Copenhagen, Denmark, GT2012-68908.

Silva, V. T., Lundbladh, A. and Xisto, C. (2022), "Aerodynamic installation effects of over-the-wing mounted ultra-high bypass engines", 25th ISABE Conference, Ottawa, Canada, ISABE-2022-145.

Smith, S., Nemec, M. and Krist, S. (2013), "Integrated nacelle-wing shape optimization for an ultra-high bypass fanjet installation on a single-aisle transport configuration", 51st AIAA Aerospace Sciences Meeting including the New Horizons Forum and Aerospace Exposition, Grapevine, TX, USA, AIAA 2013-0543.

Stańkowski, T. P., MacManus, D. G., Sheaf, C. T. and Christie, R. (2016), "Aerodynamics of aero-engine installation", *Proceedings of the Institution of Mechanical Engineers, Part G: Journal of Aerospace Engineering*, Vol. 230 No. 14, pp. 2673-2692, doi: 10.1177/0954410016630332.

Sutherland, W. (1893), "LII. The viscosity of gases and molecular force", *The London, Edinburgh, and Dublin Philosophical Magazine and Journal of Science*, Vol. 36 No. 233, pp. 507-531, doi: 10.1080/14786449308620508.

Swarthout, A., MacManus, D., Tejero, F. and Matesanz-Garcia, J. (2023), "Aerodynamics of a compact nacelle at take-off conditions", AIAA Aviation Forum, San Diego, CA, USA, AIAA 2023-3309, doi: 10.2514/6.2023-3309.

Tejero, F., Goulos, I., MacManus, D. G. and Sheaf, C. (2023), "Propulsion integration study of civil aero-engine nacelles", *The Aeronautical Journal*, in-press.

Tejero, F., MacManus, D., Hueso-Rebassa, J., Sanchez-Moreno, F., Goulos, I. and Sheaf, C. (2022a), "Aerodynamic optimisation of civil aero-engine nacelles by dimensionality reduction and multi-fidelity techniques", *International Journal of Numerical Methods for Heat & Fluid Flow*, Vol. ahead-of-print, doi: 10.1108/HFF-06-2022-0368.

Tejero, F., MacManus, D. G., Matesanz-Garcia, J., Swarthout, A. and Sheaf, C. (2022b), "Towards the design and optimisation of future compact aero-engines: intake/fancowl trade-off investigation", *International Journal of Numerical Methods for Heat & Fluid*, Vol. ahead-of-print, doi: 10.1108/HFF-06-2022-0366.

Vassberg, J. C., Tinoco, E. N., Mani, M., Rider, B., Zickuhr, T., Levy, D. W., Brodersen, O. P., Eisfeld, B., Crippa, S., Wahls, R. A., Morrison, J. H., Mavriplis, D. J. and Murayama, M. (2014), "Summary of the fourth AIAA computational fluid dynamics drag prediction workshop", *Journal of Aircraft*, Vol. 51 No. 4, pp. 1070-1089, doi: 10.2514/6.2010-4547.

Vermeersch, O. and Bouteiller, X. (2014), "Numerical study of laminar nacelles: natural and hybrid laminar flow design", *International Journal of Engineering Systems Modelling and Simulation*, Vol. 6 No. 3-4, pp. 191-204, doi: 10.1504/IJESMS.2014.063124.

Wiart, L., Atinault, O., Paluch, B., Hue, D. and Grenon, R. (2015), "Development of NOVA aircraft configurations for large engine integrations studies", 33rd AIAA Aplied Aerodynamic Conference, Dallas, TX, USA, AIAA 2015-2254.

Zachos, P. K. (2013), "Modelling and analysis of turbofan engines under windmilling conditions", *Journal of Propulsion and Power*, Vol. 29 No. 4, pp. 882-890, doi: 10.2514/1.B34729.

Zhang, M. H., Meng, X. X., Wang, M. L., Wang, H., Bai, J. Q. and Nie, S. Y. (2022), “Fluid mechanic analysis on the interaction between natural laminar flow nacelle and wingbody on a transonic aircraft”, *AIP Advances*, Vol. 12, doi: 10.1063/5.0122064.

Installed nacelle aerodynamics at cruise and windmilling conditions

Sánchez-Moreno, Francisco

2024-07-11

Sánchez-Moreno F, MacManus D, Tejero F, et al., (2024) Installed nacelle aerodynamics at cruise and windmilling conditions. Aircraft Engineering and Aerospace Technology, Volume 96, Issue 6, August 2024, pp. 757-768

https://doi.org/10.1108/AEAT-03-2023-0070